Materials Advances

ROYAL SOCIETY OF CHEMISTRY

PAPER

View Article Online
View Journal

Cite this: DOI: 10.1039/d6ma00112b

Copper immobilized on a layered magnetite-based nanocatalyst for sustainable Ullmann cross-coupling reaction

Eden Sinchana D Souza and Aatika Nizam *

Received 23rd January 2026,
Accepted 23rd March 2026

DOI: 10.1039/d6ma00112b

rsc.li/materials-advances

This study demonstrates the efficient synthesis of diarylthioethers *via* C–S cross-coupling between diverse aryl halides and arylthiols utilizing a magnetically retractable Fe_3O_4@SiO_2–$PrNH_2$–SA–Cu(II) nanocatalyst using K_2CO_3 as a base in DMF. The heterogeneous nanocatalyst was fabricated through a multistep process. The designed catalyst was characterized using various techniques, such as XRD, HRTEM, FESEM, STEM, EDAX, elemental mapping, TGA, VSM, XPS, ICP-OES and FT-IR. The catalyst design provides a dual role of the Schiff base-anchoring copper ions, to accelerate the oxidative addition and reductive elimination steps. This method makes use of ligand-free synthesis of diarylsulfides, enabling magnetic recovery and reuse of the catalyst for up to 6 cycles. The nanocatalyst exhibited high catalytic activity and a broad substrate scope. The magnetic nature of the nanocatalyst enabled easy separation from the reaction mixture using an external magnet, thus simplifying the workup. The synthesized nanocatalyst was then utilized for the synthesis of diarylthioethers and heterodiarylthioethers. The pure compounds were characterized using ^1H and ^{13}C NMR. This catalytic system offers a cost-effective, efficient, and simple protocol for the formation of the C–S bond.

1 Introduction

Diarylsulfides represent an important class of organosulfur compounds with significant effects in pharmaceuticals,[1–8] agrochemicals, and materials science.[9–16] Structurally, they feature an aryl-*S*-aryl linkage with sulfur as a heteroatom, which exhibits unique electronic and steric properties essential for bioactive molecules such as anticancer agents,[17] antifungal drugs,[18] and kinase inhibitors.[19] Traditionally, the synthesis of diarylthioethers utilized transition metal-catalyzed C–S cross coupling, typically employing palladium or copper metal complexes to couple arylhalides and arylthiols.[20–22] However, these approaches face significant limitations, including harsh chemical conditions and the use of expensive ligands.[23] For example, palladium catalysts often require inert atmospheres and high temperatures, while copper catalysts in homogeneous systems suffer poor recyclability and metal leaching, making it difficult for purification and increasing costs. Also, common sources of aryl thiols have a foul smell, demanding careful handling.[24–26] These challenges highlight the need for sustainable, efficient catalytic systems that operate under mild conditions, minimize environmental impact, and align with green chemistry principles. In response, nanocatalysts have emerged as transformative tools that comprise high surface area and tunable active sites. Magnetic nanoparticles (MNPs), particularly Fe_3O_4 cores functionalized with silica and organic ligands, offer a platform for immobilizing catalytic metals, enabling fast recovery *via* external magnets.[27–30] Copper-based nanocatalysts are especially attractive due to their abundance, low toxicity, and effectiveness in promoting C–S bond formation. The design of Fe_3O_4@SiO_2–$PrNH_2$–SA–Cu(II) integrates multiple advantages: (i) the Fe_3O_4 core permits magnetic separation; (ii) the SiO_2 shell, being inert, prevents unwanted aggregation and provides hydroxyl groups for functionalization;[31–33] (iii) the $PrNH_2$–SA Schiff base acts as a chelating ligand, stabilizing Cu ions and enhancing catalytic activity.[34] Prior studies confirm that such immobilized Cu complexes facilitate Ullmann-type coupling with high atom economy, while the magnetic support prevents difficult filtration and reduces metal leaching.[35–37] Various researchers have reported the synthesis of diarylsulfides using different nanocatalysts, as shown in Scheme 1. In 2020, Yu *et al.* and co-workers reported the synthesis of diarylsulfides using a nanocatalyst made of manganese oxide octahedral molecular sieves modified with copper ions using a ligand-free condition.[38] In 2022, Xu *et al.* and coworkers reported the synthesis of diarylthioethers using arylhalides and diaryldisulfide in the presence of a magnetic nanocatalyst synthesized by the immobilization of a palladium(II) complex on the surface of silica-coated iron oxide modified with a 2-aminopyridine ligand.[39] Building on these advances, we report a magnetically recoverable nanocatalyst Fe_3O_4@SiO_2–$PrNH_2$–SA–Cu(II) for synthesizing diarylsulfides *via*

Department of Chemistry, Christ University, Bengaluru-560029, India.
E-mail: aatika.nizam@christuniversity.in

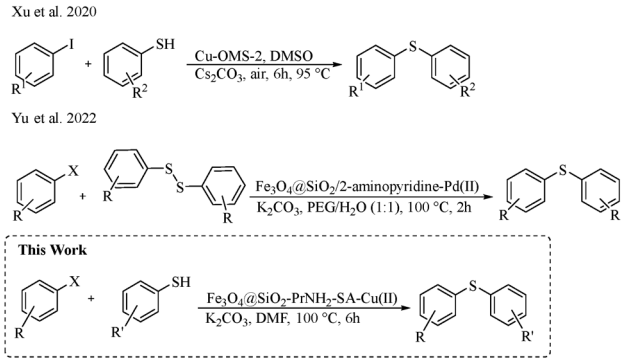

Scheme 1 Existing reports on the synthesis of diarylsulfides.

cross-coupling of arylhalides (X = Cl and Br) and arylthiols. The reaction employs K_2CO_3 as a mild, inexpensive base and DMF as a polar aprotic solvent, ensuring broad substrate compatibility under aerobic conditions. The catalyst design provides a dual role of the Schiff base-anchoring copper ions, to accelerate the oxidative addition and reductive elimination steps. Key innovations include: (i) eliminating the use of ligands and simplifying the reaction setup, (ii) achieving the product under mild conditions, and (iii) enabling magnetic recovery of the catalyst and simplifying the workup procedure, and (iv) reuse for up to 6 cycles.

2. Experimental

2.1. Materials and methods

All the chemicals were brought from Merck and Avra (India) and were used without any purification. Fourier transform infrared spectra were recorded on a Shimadzu IR Spirit spectrophotometer, and the XRD data were recorded on a Miniflex 600 diffractometer using CuK_α radiation in the range of 0°–40° (2 theta). An EZ-7 Vibrating Sample Magnetometer was used to assess the magnetic properties. The progress of the reaction and determination of the pure compounds were done by thin-layer chromatography (silica gel 60 F_{254} plates, Merck). The pure compounds were isolated using column chromatography. The TGA was carried out using the NJA-STA 2500 Regulus Simultaneous TGA/DTA Analyzer. The pure organic compounds were characterized by using ^1H and ^{13}C NMR, taking TMS as a reference. The purity of the synthesized compounds was monitored on silica gel 60 F_{254} plates purchased from Merck to monitor the reactions.

2.1.1. Preparation of Fe_3O_4 nanoparticles. The magnetic nanoparticles were synthesized according to the method reported by Chicea *et al.*[40] 2.1 mmol of $FeCl_3{\cdot}6H_2O$ and 1 mmol of $FeCl_2{\cdot}4H_2O$ in 100 mL distilled water were ultrasonicated for 30 minutes. The mixture was heated at 80 °C. Then, 10 mL of 25% aq. NH_3 was added to the mixture dropwise under a nitrogen atmosphere until a black precipitate was formed, followed by stirring for 30 minutes. The resulting precipitate was magnetically extracted from the solution, and the supernatant liquid was decanted. The solid was then washed with distilled water to remove excess base, followed by EtOH to remove other impurities. Later, it was dried at 65 °C for 12 h.

2.1.2. Preparation of silica-coated magnetic nanoparticles (Fe_3O_4@SiO_2). This coating was done according to the famous Stober method.[41] 1 g of Fe_3O_4 nanoparticles was dispersed in a 1 : 2 ratio of distilled water (20 mL) and ethanol (40 mL) while stirring at room temperature. After 10 minutes, 0.7 mL of tetraethyl orthosilicate was added dropwise and stirred at room temperature for 8 h. The resultant product was collected *via* an external magnet. It was then washed thoroughly with distilled water and then with EtOH and dried at 70 °C for 12 h under vacuum.

2.1.3. Preparation of Fe_3O_4@SiO_2–$PrNH_2$. 1 g of Fe_3O_4@SiO_2 was dispersed in 40 mL of toluene and stirred at room temperature.[42] After the dispersion of the compound uniformly, 1 mmol of (3-aminopropyl)triethoxysilane was added dropwise, and the mixture was refluxed for 24 h. The solid was extracted using an external magnet, washed with toluene to remove unreacted silane, followed by EtOH, and dried at 70 °C for 12 h under vacuum.

2.1.4. Preparation of Fe_3O_4@SiO_2–$PrNH_2$–SA. 1 g of Fe_3O_4@SiO_2–$PrNH_2$ was dispersed in 40 mL of toluene while stirring at room temperature. After the complete dispersion of the compound, 3 mmol of salicylaldehyde (SA) was added to it dropwise and then refluxed for 24 h. The solid was extracted using a magnet and washed thoroughly using toluene, followed by EtOH. Later, it was dried at 70 °C for 12 h under vacuum.

2.1.5. Doping of copper onto Fe_3O_4@SiO_2–$PrNH_2$–SA–Cu(II). 1 g of Fe_3O_4@SiO_2–$PrNH_2$–SA was added to 40 mL of DMSO while sonicating at room temperature. After uniform dispersion, 3 mmol of copper acetate was dispersed in a DMSO solution, and the mixture was refluxed for 24 h. The resultant mixture was collected using an external magnet, washed with distilled water to remove unreacted copper acetate, followed by

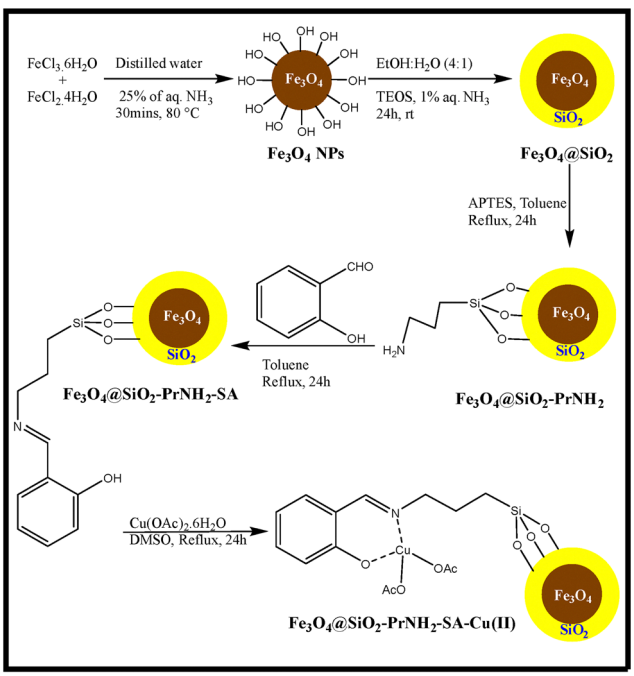

Scheme 2 Stepwise synthesis of the Fe_3O_4@SiO_2–$PrNH_2$–SA–Cu(II) nanocatalyst.

EtOH, and dried under vacuum at 70 °C for 12 h. This is denoted as Fe_3O_4@SiO_2–$PrNH_2$–SA–Cu(II) (Scheme 2).

2.1.6. General procedure for C–S cross coupling reaction using Fe_3O_4@SiO_2–$PrNH_2$–SA–Cu(II). 0.025 mmol of Fe_3O_4@SiO_2–$PrNH_2$–SA–Cu(II) was added to a mixture of aryl halide (1 mmol), arylthiols (1.2 mmol), and K_2CO_3 (2 mmol) in DMF under a N_2 atmosphere. The progress of the reaction was monitored by TLC. After the completion of the reaction (monitored by TLC), the reaction mixture was diluted with ethyl acetate. Later, the nanocatalyst was magnetically removed, washed with ethyl acetate, and used for subsequent runs. The organic layer was washed thoroughly with water and dried over anhydrous sodium sulfate. The solvent was evaporated, and the resulting crude was purified by column chromatography to afford the pure product.

3. Results and discussion

3.1. Characterization techniques

The structure of the fabricated Fe_3O_4@SiO_2–$PrNH_2$–SA–Cu(II) was characterized using various characterization techniques, such as FESEM, STEM, HRTEM, VSM, XRD, FTIR, EDAX, XPS, ICP-OES, elemental mapping, and TGA.

3.1.1. FESEM and STEM analysis. Fig. 1(a) and (b) show the FESEM image of the catalyst. The particles appear irregular and closely-packed, showing the successful surface modification. These images demonstrate a compact surface morphology of the nanocatalyst, indicating successful layer-by-layer functionalization. The SiO_2 coating and other organic groups likely increased the surface roughness.[43,44] Fig. 1(c) and (d) are dark-field STEM images. This combined data provides evidence of successful surface modification and metal incorporation. Fig. 2 shows the size distribution analysis of the synthesized nanocatalyst.

3.1.2. High-resolution transmission electron microscopy (HRTEM). Fig. 3(a) and (b) show the HRTEM images of the synthesized nanocatalyst Fe_3O_4@SiO_2–$PrNH_2$–SA–Cu(II) at 20 nm magnification. The images reveal that the particles possess quasi-spherical morphology.

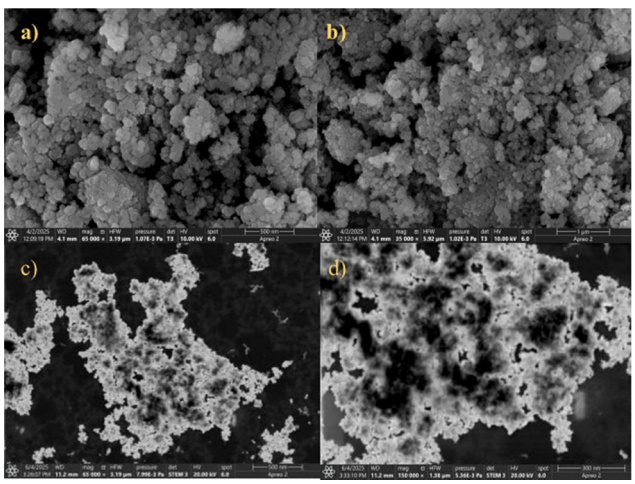

Fig. 1 (a) and (b) represent FESEM images, and (c) and (d) represent STEM images of Fe_3O_4@SiO_2-$PrNH_2$-SA-Cu(II).

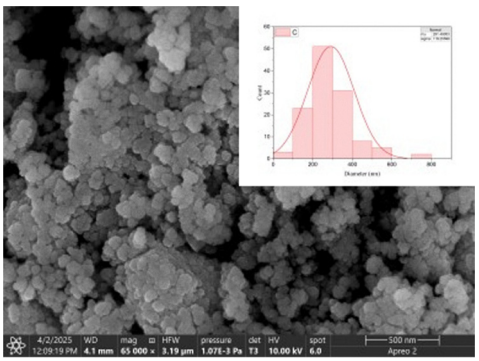

Fig. 2 Size distribution chart of the nanocatalyst.

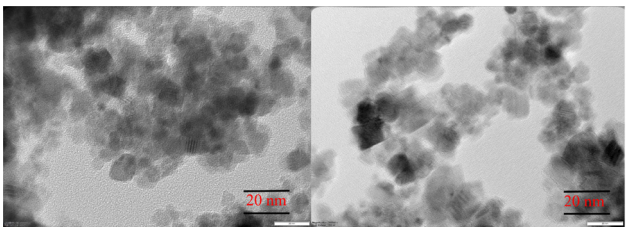

Fig. 3 HRTEM images of Fe_3O_4@SiO_2-$PrNH_2$-SA-Cu(II).

3.1.3. Energy dispersive X-ray analysis (EDAX). EDAX of the Fe_3O_4@SiO_2–$PrNH_2$–SA–Cu(II) nanocatalyst was carried out to confirm the presence of the elements present in it (Fig. 4). The EDAX data shows the presence of Fe, Si, O, N, C, and Cu in the sample. According to the data, the elements C, N, O, Si, Fe, and Cu have atom percentages of 18.5%, 4.46%, 47.1%, 1.4%, 25.25%, and 3.29%, respectively. Also, the K_α values of carbon and nitrogen are nearly identical, so the nitrogen signal overlaps with that of carbon in the image. This confirms the successful deposition of all the elements in the nanocatalyst.

3.1.4. Elemental mapping. To further confirm the elements present in the sample, elemental mapping was performed (Fig. 5). This analysis helps in visualizing and analyzing the distribution of elements within the nanocatalyst. The results demonstrate how the elements are dispersed and

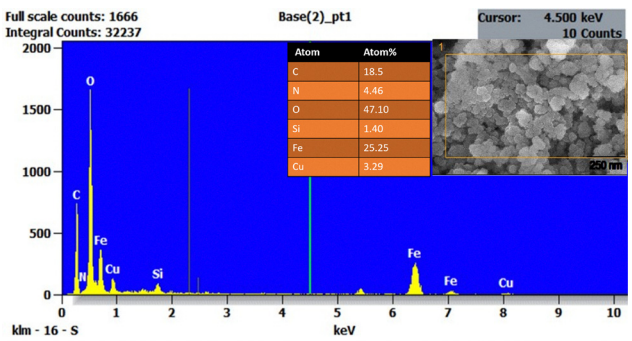

Fig. 4 EDAX data of the Fe_3O_4@SiO_2-$PrNH_2$-SA-Cu(II) nanocatalyst showing the expected elements.

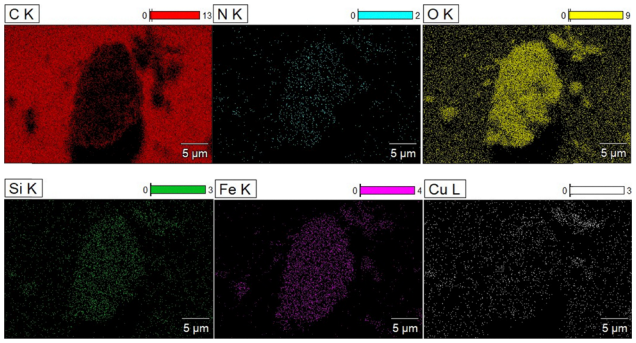

Fig. 5 Elemental mapping of the synthesized Fe_3O_4@SiO_2–$PrNH_2$–SA–Cu(II) nanocatalyst.

confirm the expected elements in the sample. Each square represents a map that shows the distribution of elements within the sample on a microscopic level. The image provides visual data of the elements: C (carbon) is shown in red, N (nitrogen) is shown in light blue, O (oxygen) is shown in yellow, Si (silicon) is shown in light green, Fe (iron) is shown in pink, Cu (copper) is shown in white. In Fig. 4, the brighter spots indicate the higher concentration of the respective element present in the sample. This data further confirms that the nanocatalyst contains all the expected elements in the sample, and it agrees with the EDAX data.

3.1.5. X-ray diffraction analysis. X-ray diffraction data of Fe_3O_4@SiO_2–$PrNH_2$–SA–Cu(II) are displayed in Fig. 6. The results of the analysis confirmed that the Fe_3O_4 nanoparticles retained their phase even after the surface modifications. The Fe_3O_4 XRD data are in good agreement with the standard value of Fe_3O_4 (JCPDS file no: 65-3107). The typical characterization peaks of Fe_3O_4 at 2θ = 30.1°, 35.4°, 43.4°, 53.53°, 57.1°, and 62.99° can be indexed to the (220), (311), (400), (422), (511), and (440) planes of Fe_3O_4 in its cubic phase, respectively. The XRD data of Fe_3O_4@SiO_2–$PrNH_2$–SA–Cu also show all the peaks of Fe_3O_4. The diffraction peak at 2θ = 35.4° shows increased intensity, indicating strong crystallinity of the catalyst due to fabrication. The XRD data obtained in this study align with literature reports.[45] The XPS analysis further confirms the presence of copper in its +2 oxidation state. A noticeable change in the shift of the diffraction peak 2θ = 57.1° to 2θ = 54.1° is due to the change in the lattice parameters. The shift in the XRD peak during doping is due to a change in the lattice parameter and is related to the ionic radius of the dopant compared to that of the host. The leftward shift of the peak indicates that the ionic radius of the Cu is slightly larger, thus increasing the interplanar spacing and shifting the peaks to lower 2θ values. Additionally, a weak diffraction peak around 32° and 67° in the XRD pattern of the Fe_3O_4 nanoparticles may be attributed to the presence of trace maghemite phase, indicating partial oxidation of Fe_3O_4 due to exposure to air. The peak intensity is less prominent after the SiO_2 coating and further surface functionalization, indicating successful core–shell modification.

3.1.6. Fourier transform infrared spectroscopy (FTIR). Fig. 7 shows the stepwise FTIR analysis of the nanocatalyst. (a) Fe_3O_4 nanoparticles, (b) Fe_3O_4@SiO_2, (c) Fe_3O_4@SiO_2–$PrNH_2$, (d) Fe_3O_4@SiO_2–$PrNH_2$–SA, and (e) Fe_3O_4@SiO_2–$PrNH_2$–SA–Cu(II). In Fig. 7a, the presence of stretching vibrations at 582 cm^{-1} is attributed to the Fe–O band. Also, the stretching vibration of adsorbed water molecules on the surface of the Fe_3O_4 nanoparticles at 3385 cm^{-1} is noticeable. This confirms the successful formation of Fe_3O_4 nanoparticles. In Fig. 7b, the broad band at around 3300 cm^{-1} is attributed to surface silanol groups (Si–OH). The Fe–O band remained intact. The stretching band at around 1089 cm^{-1} is attributed to the Si–O–Si bond. This confirms the condensation reaction between the hydroxyl groups of Fe_3O_4 and the alkoxysilane of TEOS. In Fig. 7c, the Fe–O and Si–O–Si stretching bands remained intact. The absorbed peak at 3400 cm^{-1} corresponds to the N–H stretching vibration of the NH_2 group of APTES. The band at around 2900 cm^{-1} is attributed to the stretching vibration of the C–H bond of the methylene group of APTES. This confirms the presence of APTES chain molecules. The presence of a band at

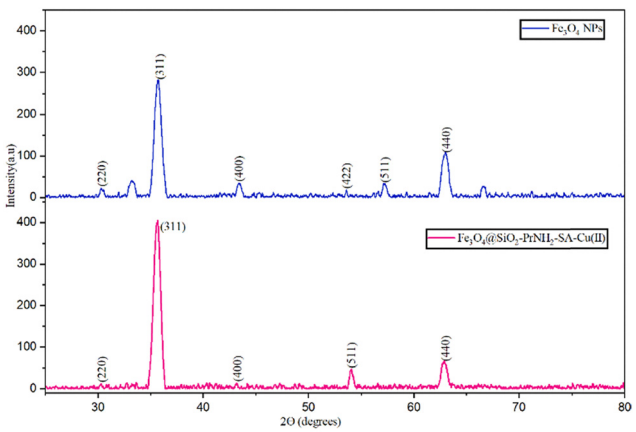

Fig. 6 XRD data of Fe_3O_4 and Fe_3O_4@SiO_2-$PrNH_2$-SA-Cu(II) nanocatalyst incorporation.

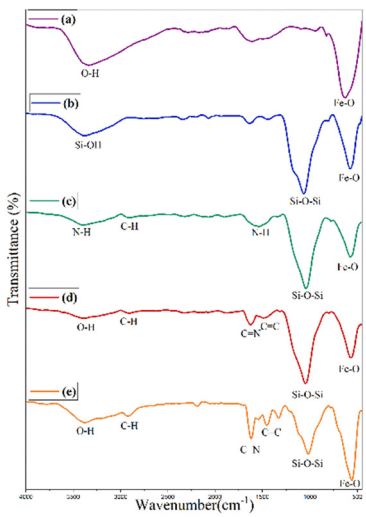

Fig. 7 FTIR spectrum of (a) Fe_3O_4 nanoparticles, (b) Fe_3O_4@SiO_2, (c) Fe_3O_4@SiO_2-$PrNH_2$, (d) Fe_3O_4@SiO_2-$PrNH_2$-SA, and (e) Fe_3O_4@SiO_2-$PrNH_2$-SA-Cu(II).

around 1439 cm^{-1} is attributed to the C–H bending mode of the methylene groups in APTES. In Fig. 7d, the presence of the characteristic C=C band of the benzene ring at 1605 cm^{-1} confirms the successful incorporation of salicylaldehyde onto Fe_3O_4@SiO_2–$PrNH_2$. The band at around 1624 cm^{-1} corresponds to the C=N stretching band, confirming the successful formation of the Schiff base. The peak at 3437 cm^{-1} corresponds to the aromatic O–H. In Fig. 7e, slight changes in the intensity of the peaks indicate the successful incorporation of copper onto the surface of Fe_3O_4@SiO_2–$PrNH_2$–SA.

3.1.7. Thermogravimetric analysis (TGA). To evaluate the thermal stability of the nanocatalyst, thermogravimetric analysis was performed (Fig. 8). The initial weight loss of approximately 3% below 190 °C is attributed to the evaporation of physically adsorbed water molecules. This is further supported by the FT-IR spectrum (Fig. 7), which displays only a weak –OH stretching band, confirming minimal moisture content on the catalyst surface. A subsequent weight loss of around 7% observed in the range of 190–370 °C is mainly due to the decomposition of the aminopropyl linkage and the Schiff base moieties. Another significant weight loss of about 4% between 470 and 610 °C is associated with the breakdown of a more thermally stable Schiff base complex with copper. Beyond 600 °C, the TGA curve becomes flat, indicating no further mass loss and confirming the presence of a thermally stable inorganic core.[46] These observations suggest that the nanocatalyst remains thermally stable up to 250 °C, making it suitable for applications in thermally demanding organic transformations.

3.1.8. Vibrating sample magnetometer (VSM) analysis. To evaluate the magnetic properties of the nanocatalyst, vibrating sample magnetometer analysis was conducted at room temperature (Fig. 9). The resulting *M–H* curve, which plots magnetic moment (emu g^{-1}) on the *Y*-axis against the applied magnetic field (O_e) along the *X*-axis, displays a nearly symmetrical S-shaped plot with a narrow hysterical loop indicating minimal energy loss during magnetization and demagnetization. The curve flattens near ±40 emu g^{-1} when the strong field is applied, indicating that the material has reached saturation magnetization (M_s).

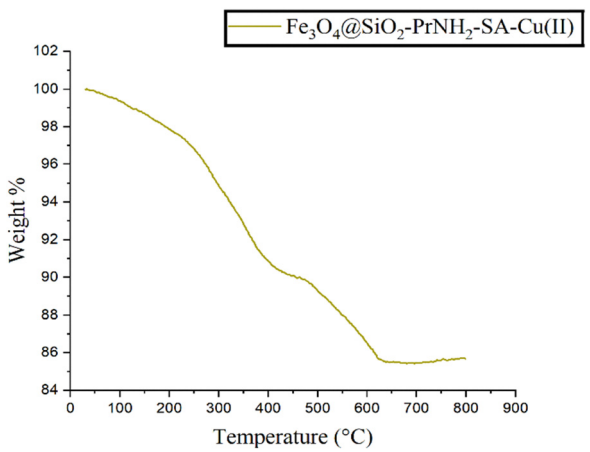

Fig. 8 Thermogravimetric analysis data of the Fe_3O_4@SiO_2-$PrNH_2$-SA-Cu(II) nanocatalyst.

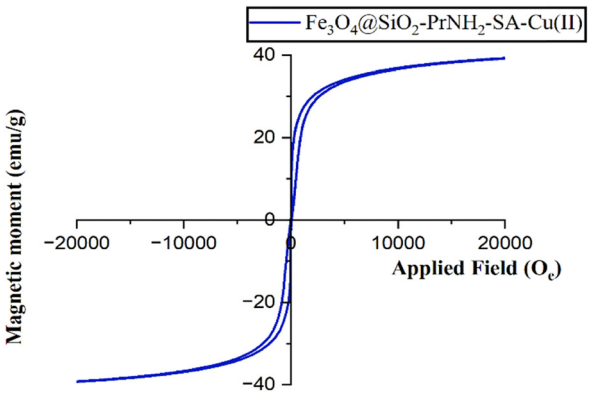

Fig. 9 VSM data of the Fe_3O_4@SiO_2-$PrNH_2$-SA-Cu(II) nanocatalyst showing the magnetic properties.

This saturation value shows that the material is strongly magnetic and can be easily separated using an external magnet. Additionally, the curve crosses the X-axis around 0–100 O_e, indicating low coercivity (H_c). This low coercivity suggests that the catalyst loses its magnetization rapidly once the external magnet field is removed, which shows that the catalyst is ideal for reusability. Overall, these characteristics indicate that the nanocatalyst exhibits supermagnetic behaviour, making it highly suitable for magnetic separation and repeated use in catalytic applications.

3.1.9. X-ray photoelectron spectroscopy (XPS). Fig. 10 shows the XPS curve of Cu 2p. The Cu 2p spectrum exhibits two predominant peaks at binding energies 933.68 eV and 953.58 eV, due to spin–orbit splitting of Cu 2p into Cu $2p_{3/2}$ and Cu $2p_{1/2}$, respectively. The satellite peaks at 942.38 eV and 962.68 eV confirm the presence of Cu^{+2} species.[47]

3.1.10. Inductively coupled plasma-optical emission spectrometry (ICP-OES). To determine the percentage of copper present in the nanocatalyst Fe_3O_4@SiO_2–$PrNH_2$–SA–Cu(II), ICP-OES analysis was carried out. It was found that the catalyst contained 5.257 wt% of copper (0.83 mmol of Cu per gram of the catalyst).

3.2. Experiments on catalytic activity

The catalytic activity of Fe_3O_4@SiO_2–$PrNH_2$–SA–Cu(II) was evaluated for C–S cross-coupling reactions. To establish the optimum reaction conditions, the influence of various parameters, such as base, solvent, and temperature, was investigated using

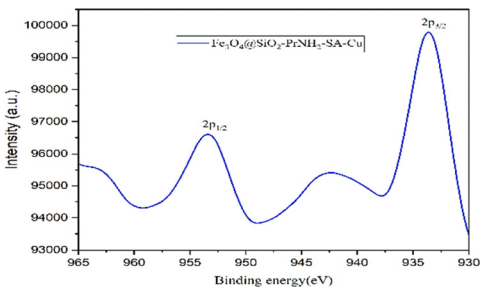

Fig. 10 XPS analysis of the Fe_3O_4@SiO_2-$PrNH_2$-SA-Cu nanocatalyst.

4-bromonitrobenzene and thiophenol as model substrates (Table 1).

The reaction conditions were optimized to achieve maximum efficiency, starting with solvent screening using 4-bromoacetophenone and thiophenol as starting materials in the presence of 0.017 mmol of catalyst load and Cs_2CO_3 as a model base. Various solvents such as DMF, DMSO, ethanol, methanol, MeCN, H_2O, ethanol:H_2O, toluene, and dioxane were examined under reflux conditions and gave 61%, 40%, 42%, 43%, 35%, 45%, 51%, 25%, and 20% yield, respectively (entries 1–7, 10 and 11). Also, DCM and THF under reflux conditions gave trace yields (entries 8 and 9). Among these, DMF demonstrated superior performance. Subsequent base optimization was performed using DMF as a solvent. Bases like Na_2CO_3, Et_3N, DBU, K_2CO_3, NaOH, KOH, and K_3PO_4 were examined and gave 54%, 15%, 11%, 69%, 58%, 54%, and 21% yield, respectively (entries 12–18). Among these, K_2CO_3 gave the highest yield of the product. With the solvent and base optimized, temperature optimization trials were conducted across the gradient (60–110 °C) to evaluate thermal effects on the reaction (entries 20–25). Again, a marked improvement occurred at 100 °C (entry 24), where the yield peaked. Later, the catalyst loading was systematically varied from 0.017 to 0.029 mmol to assess its impact on the yield. A marked improvement was observed at a catalyst load of 0.025mmol (entry 29). A clear correlation was observed: increasing the catalyst from 0.017 to 0.029 mmol progressively improved the yield, suggesting that sufficient catalytic sites were critical for driving the reaction to completion. Collectively, the starting materials with K_2CO_3 as the base in DMF solvent, a catalyst load of 0.025 mmol, and a reaction temperature of 100 °C were selected. Under the optimized reaction conditions, the scope of this method was further investigated using various substituted arylhalides and substituted arylthiols to afford aryl-substituted diarylsulfides. Various derivatives of diarylsulfides were synthesized. Various monosubstituted aryl halides (X = Br and Cl) and arylthiols were investigated. Scheme 3 shows the various diarylsulfide derivatives synthesized.

The substrate scope of the reaction was investigated using various bromo-substituted arylhalides and arylthiols, such as thiophenol, *p*-chlorothiophenol, *p*-tolylthiophenol, and *p*-nitrothiophenol. Initially, thiophenol **2a** was employed as a thiol partner with different aryl bromides. The coupling of *p*-bromobenzonitrile afforded diarylsulfide **3a** in 90% yield. Similarly, *p*-bromonitrobenzene afforded **3d** in 92% yield, and *p*-bromobenzaldehyde produced **3g** in 87% yield.

Table 1 Optimization of the C–S coupling reaction conditions using Fe_3O_4@SiO_2–$PrNH_2$–SA–Cu(II)

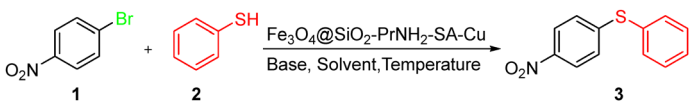

1 2 3

S. no.	Catalyst load (mmol)	Base	Solvent	Temperature (°C)	Yield[b] (%)
1	0.017	Cs_2CO_3 (1.5 mmol)	DMF	Reflux	61
2	0.017	Cs_2CO_3 (1.5 mmol)	DMSO	Reflux	40
3	0.017	Cs_2CO_3 (1.5 mmol)	Ethanol	Reflux	42
4	0.017	Cs_2CO_3 (1.5 mmol)	Methanol	Reflux	43
5	0.017	Cs_2CO_3 (1.5 mmol)	MeCN	Reflux	35
6	0.017	Cs_2CO_3 (1.5 mmol)	H_2O	Reflux	45
7	0.017	Cs_2CO_3 (1.5 mmol)	Ethanol : H_2O (1 : 1)	Reflux	51
8	0.017	Cs_2CO_3 (1.5 mmol)	DCM	Reflux	Traces
9	0.017	Cs_2CO_3 (1.5 mmol)	THF	Reflux	Traces
10	0.017	Cs_2CO_3 (1.5 mmol)	Toluene	Reflux	25
11	0.017	Cs_2CO_3 (1.5 mmol)	Dioxane	Reflux	20
12	0.017	Na_2CO_3 (1.5 mmol)	DMF	Reflux	54
13	0.017	Et_3N (1.5 mmol)	DMF	Reflux	15
14	0.017	DBU (1.5 mmol)	DMF	Reflux	11
15	0.017	K_2CO_3 (1.5 mmol)	DMF	Reflux	69
16	0.017	NaOH (1.5 mmol)	DMF	Reflux	58
17	0.017	KOH (1.5 mmol)	DMF	Reflux	54
18	0.017	K_3PO_4 (1.5 mmol)	DMF	Reflux	21
19[a]	—	K_2CO_3 (1.5 mmol)	DMF	Reflux	No reaction
20	0.017	K_2CO_3 (1.5 mmol)	DMF	60	24
21	0.017	K_2CO_3 (1.5 mmol)	DMF	70	36
22	0.017	K_2CO_3 (1.5 mmol)	DMF	80	51
23	0.017	K_2CO_3 (1.5 mmol)	DMF	90	70
24	0.017	K_2CO_3 (1.5 mmol)	DMF	100	80
25	0.017	K_2CO_3 (1.5 mmol)	DMF	110	80
26	0.017	K_2CO_3 (1.8 mmol)	DMF	100	85
27	0.017	K_2CO_3 (2 mmol)	DMF	100	88
28	0.021	K_2CO_3 (2 mmol)	DMF	100	90
29	**0.025**	**K_2CO_3 (2 mmol)**	**DMF**	**100**	**92**
30	0.029	K_2CO_3 (2 mmol)	DMF	100	92
31	Fe_3O_4@SiO_2–$PrNH_2$	K_2CO_3 (2 mmol)	DMF	100	No reaction
32	Fe_3O_4@SiO_2–$PrNH_2$–SA	K_2CO_3 (2 mmol)	DMF	100	No reaction

Reaction conditions: 4-bromobenzonitrile (1 mmol), thiophenol (1.2 mmol), solvent (3 mL). [a] Without nanocatalyst. [b] Isolated yield.

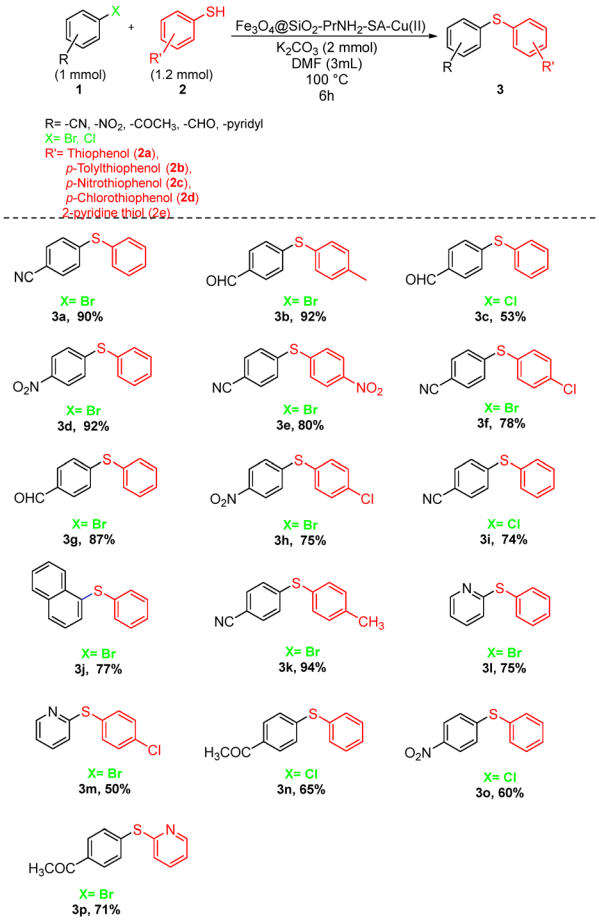

Scheme 3 Synthesis of diarylthioethers using the optimized reaction conditions.

Later, we checked the scope with 1-bromonapthalene with **2a.** The coupled sterically hindered product **3j** was obtained in 77% yield. The reactions with heteroaryl substrate 1-bromopyridine and **2a** furnished the product **3l** in 75% yield, respectively. To further assess the reactivity of halides, chloro-substituted aryl halides were investigated. The coupling of *p*-chlorobenzaldehyde with thiophenol provided product **3c** in 53% yield, while *p*-chlorobenzonitrile afforded **3i** in 74% yield. The reaction of 4-chloroacetophenone with thiophenol furnished **3n** in 65% yield. The C–Cl bond requires a higher activation energy to undergo oxidative addition compared to the C–Br bond. Additionally, the lower yield with the –CHO and –CN derivatives is likely due to the relatively poor leaving ability of the chloride ion. Next, the scope was extended to other arylthiols. The reaction of *p*-tolylthiophenol **2b** with *p*-benzonitrile and *p*-bromobenzaldehyde afforded **3k** and **3b** in 94% and 92% yield, respectively, whereas the same aryl bromide with *p*-nitrothiophenol yielded **3e** in 80% yield. The coupling of *p*-bromonitrobenzene with *p*-chlorothiophenol gave **3h** in 75% yield, and *p*-bromobenzonitrile with *p*-chlorothiophenol produced **3f** in 78% yield. Finally, heteroarylthiols were explored. The reaction of 1-bromopyridine with **2d** and *p*-bromoacetophenone with **2e** afforded **3m** and **3p** in 50% and 71% yield, respectively. The reduced yield may be attributed to steric hindrance around the reactive sites.

4. Test for reusability and heterogeneity

To evaluate the catalytic efficiency and reusability of the synthesized nanocatalyst Fe_3O_4@SiO_2–$PrNH_2$–SA–Cu(II), a recycling study was performed using 4-bromobenzonitrile with *p*-tolylthiophenol. Upon completion of each reaction cycle (monitored by TLC), the mixture was diluted with ethyl acetate to extract the organic components. The nanocatalyst was then separated using an external magnet, washed thoroughly with ethyl acetate, followed by ethanol to remove any impurities, and dried before further use. This regenerated catalyst was subsequently used in the next cycle under similar conditions. It was observed that the catalyst retained its activity and provided high yields for up to 6 consecutive cycles. However, the activity dropped in the 7th cycle indicating the loss of reactive sites over repeated use (Fig. 11). Approximately 93–97% of the catalyst was recovered after each cycle, indicating efficient recovery and good stability. The changes in peak intensity in the FT-IR and XRD data, shown in Fig. 12 and 13, respectively, indicate the loss of the originally fabricated nanostructure. The FTIR spectrum shows noticeable variation in the characteristic bands corresponding to C═N, Fe–O, and Si–O–Si, confirming the loss of the coating, and XRD data align with this. This is most likely due to the structural degradation of surface functional groups and leaching of Cu(II) species. This is further confirmed by FESEM data shown in Fig. 14. The change in the surface of the nanocatalyst was observed, and the quasi-spherical shape was no longer preserved. The surface seems to be rough, and this can be attributed to the copper leaching and the surface being covered with organic moieties. This interpretation is further supported by EDAX data shown in Fig. 15.

A hot filtration test was performed under the optimized reaction conditions (Fig. 16). After 1 h, the nanocatalyst was magnetically separated from the reaction mixture, and the filtrate was allowed to react further. No additional increase in the yield of the product was observed, which is consistent with the results of entry 19 (Table 1) and confirms the heterogeneous nature of the nanocatalyst.

5. Plausible mechanism

A plausible mechanism for the diarylsulfide synthesis is shown in Scheme 4.[45] In the first step, the oxidative addition of an

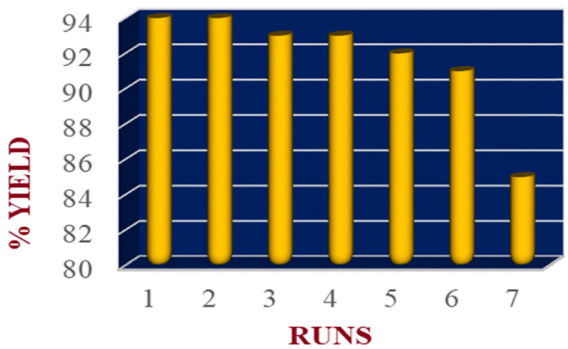

Fig. 11 Reusability test of the Fe_3O_4@SiO_2-$PrNH_2$-SA-Cu(II) nanocatalyst.

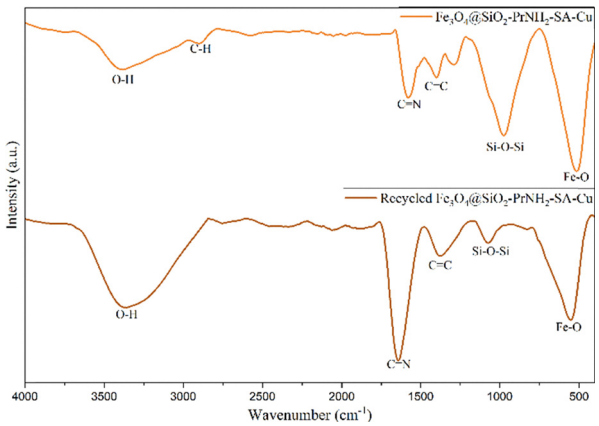

Fig. 12 Comparative FT-IR spectra of the synthesized Fe_3O_4@SiO_2-$PrNH_2$-SA-Cu(II) nanocatalyst and recycled Fe_3O_4@SiO_2-$PrNH_2$-SA-Cu(II) nanocatalyst after the 7th cycle.

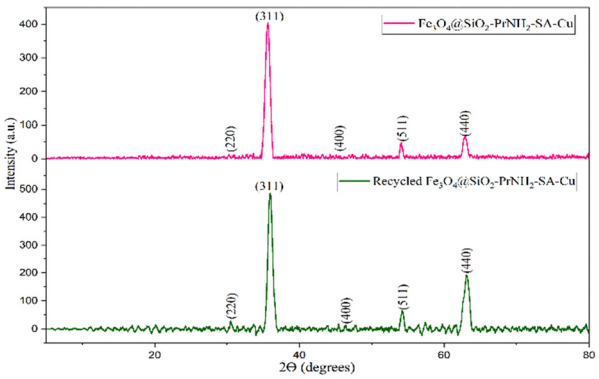

Fig. 13 Comparative XRD data of the synthesized Fe_3O_4@SiO_2-$PrNH_2$-SA-Cu(II) and recycled Fe_3O_4@SiO_2-$PrNH_2$-SA-Cu(II) after the 7th cycle.

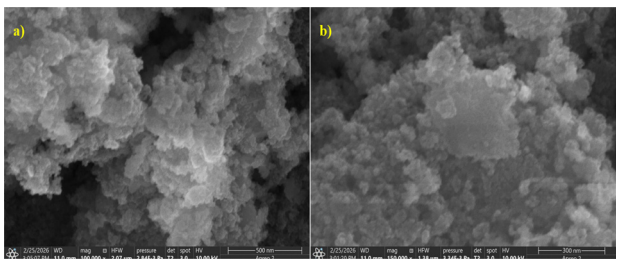

Fig. 14 FESEM image of the recycled Fe_3O_4@SiO_2-$PrNH_2$-SA-Cu(II) nanocatalyst.

arylhalide with the catalyst yields **Intermediate 1**. The base abstracts a proton from the arylthiol and generates an arylthiolate ion. The arylthiolate ion generated undergoes nucleophilic coordination with **Intermediate 1**, to yield **Intermediate 2**. **Intermediate 2** undergoes reductive elimination to give diarylsulfides and thus regenerates the nanocatalyst.

In Table 2, various nanocatalysts reported for C–S cross-coupling reactions are listed. Although the catalysts operate at lower reaction temperatures, they have certain drawbacks, including metal leaching, complex separation methods, harsh

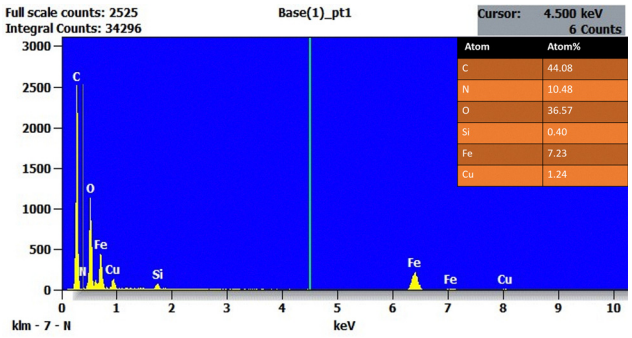

Fig. 15 EDAX analysis of the recycled catalyst.

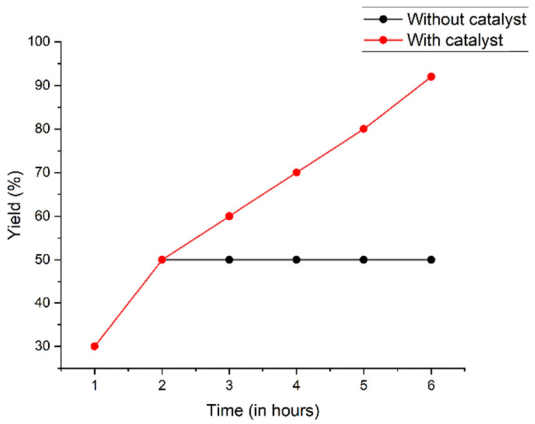

Fig. 16 Test for heterogeneity of the catalyst.

reaction conditions, and limited recyclability. In contrast, the Fe_3O_4@SiO_2–$PrNH_2$–SA–Cu(II) catalyst synthesized has merits over the others reported. This catalyst effectively overcomes the drawbacks by combining magnetic recoverability with a stable

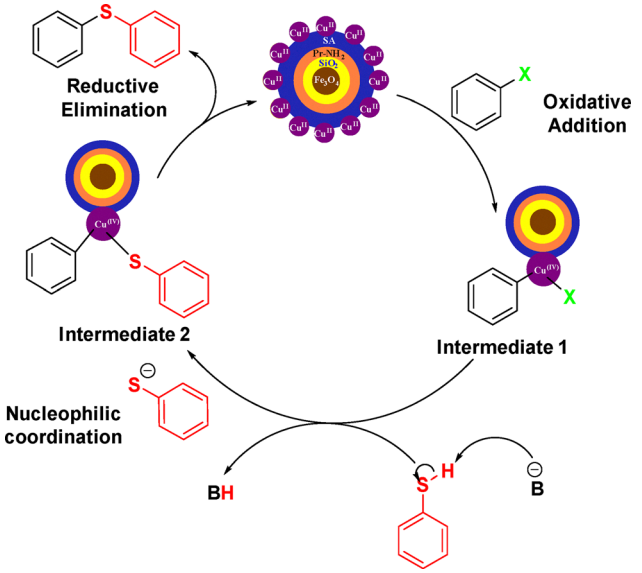

Scheme 4 Synthesis of diarylthioethers using the optimized reaction conditions.

Table 2 Comparison of the catalytic activity of the Fe_3O_4@SiO_2–$PrNH_2$–SA–Cu(II) nanocatalyst with other reported catalysts

S. no.	Nanocatalyst	Conditions	Ref.
1	$CuFe_2O_4$ MNPs	Na_2CO_3, PEG, 40 °C	48
2	M–MCM-41@TU–ZrO	PEG200, KOH, 80 °C	49
3	Fe_3O_4@SBTU@Ni(II)	DMSO, KOH, 130 °C	50
4	Pd@COF–TB	DIPEA, DMF, 120 °C	51
5	Fe_3O_4@SiO_2–$PrNH_2$–SA–Cu(II)	K_2CO_3, DMF, 100 °C	This work

SiO_2 coating and strong chelation of Schiff-base and Cu(II) centres. This structural design minimizes the metal leaching as well as ensures the formation of a coupled product in higher yields and recycled up to 6 cycles. Thus, the synthesized catalyst is found to be stable, reusable, and sustainable, making it a good choice for catalytic applications.

6 Conclusions

The Fe_3O_4@SiO_2–$PrNH_2$–SA–Cu(II) nanocatalyst has been successfully developed for the sustainable C–S cross coupling of arylhalides and arylthiols using optimized reaction conditions. The nanocatalyst exhibits high catalytic activity with a broad substrate scope. The magnetically separable nature of the nanocatalyst facilitates effortless recovery and allows it to be reused for up to 6 consecutive cycles without much loss in activity. This catalytic system eliminates the use of toxic and expensive ligands and catalysts, relying instead on a low-cost, copper-based Schiff base framework supported on a silica-coated magnetic core. The novelty of this work lies in its potential to address the key challenges, such as high catalyst cost, and tedious separation of the catalyst. By integrating all the properties of the catalyst, such as magnetic, heterogeneous nature, and cost-effective method, this method offers an industrially feasible alternative to traditional cross-coupling reactions. The catalytic activity can be explored for other C-heteroatom coupling reactions, such as C–O and C–N. By further optimizing the reaction conditions for aqueous or solvent-free media to enhance sustainability, its potential for large-scale applications can be explored.

Author contributions

Eden Sinchana D. Souza: conceptualization, investigation, formal analysis, and writing – original draft. Aatika Nizam: conceptualization, data curation, validation, resources, formal analysis, project administration, supervision, and writing – original draft.

Conflicts of interest

There are no conflicts to declare.

Data availability

The data supporting this article have been included as part of the supplementary information (SI). Supplementary information is available. See DOI: https://doi.org/10.1039/d6ma00112b.

Acknowledgements

The authors would like to acknowledge Christ University for providing a laboratory facility for performing experiments. Furthermore, the authors would like to acknowledge Indian Institute of Technology Bombay, Powai, The Gandhigram Rural Institute (Deemed to be University), Tamil Nadu, Pondicherry University, Pondicherry, and Alagappa University, Tamil Nadu, for recording the datas.

References

1 J. Krapcho, E. R. Spitzmiller and C. F. Turk, *J. Med. Chem.*, 1963, **6**, 544–546.
2 J. Krapcho and C. F. Turk, *J. Med. Chem.*, 1966, **9**, 191–195.
3 N. S. Gunasekara and C. M. Spencer, *CNS Drugs*, 1998, **9**, 325–340.
4 H. X. Ding, K. K.-C. Liu, S. M. Sakya, A. C. Flick and C. J. O'Donnell, *Bioorg. Med. Chem.*, 2013, **21**, 2795–2825.
5 B. P. Chekal, S. M. Guinness, B. M. Lillie, R. W. McLaughlin, C. W. Palmer, R. J. Post, J. E. Sieser, R. A. Singer, G. W. Sluggett, R. Vaidyanathan and G. J. Withbroe, *Org. Process Res. Dev.*, 2014, **18**, 266–274.
6 M. Feng, B. Tang, S. H. Liang and X. Jiang, *Curr. Top. Med. Chem.*, 2016, **16**, 1200–1216.
7 E. Rufino-Felipe, H. Valdés and D. Morales-Morales, *Eur. J. Org. Chem.*, DOI: 10.1002/ejoc.202200654.
8 S. Jammi, S. Sakthivel, L. Rout, T. Mukherjee, S. Mandal, R. Mitra, P. Saha and T. Punniyamurthy, *J. Org. Chem.*, 2009, **74**, 1971–1976.
9 A. Mishra, C.-Q. Ma and P. Bäuerle, *Chem. Rev.*, 2009, **109**, 1141–1276.
10 H. Bürckstümmer, A. Weissenstein, D. Bialas and F. Würthner, *J. Org. Chem.*, 2011, **76**, 2426–2432.
11 K. Takimiya, S. Shinamura, I. Osaka and E. Miyazaki, *Adv. Mater.*, 2011, **23**, 4347–4370.
12 T. Okamoto, C. Mitsui, M. Yamagishi, K. Nakahara, J. Soeda, Y. Hirose, K. Miwa, H. Sato, A. Yamano, T. Matsushita, T. Uemura and J. Takeya, *Adv. Mater.*, 2013, **25**, 6392–6397.
13 T. Mori, T. Nishimura, T. Yamamoto, I. Doi, E. Miyazaki, I. Osaka and K. Takimiya, *J. Am. Chem. Soc.*, 2013, **135**, 13900–13913.
14 K. Takimiya, I. Osaka, T. Mori and M. Nakano, *Acc. Chem. Res.*, 2014, **47**, 1493–1502.
15 E. S. D. Souza, S. Hegde, A. Nizam and V. V. Lakshmaiah, *Asian J. Org. Chem.*, DOI: 10.1002/ajoc.202500266.
16 E. S. D. Souza and A. Nizam, *Catal. Today*, 2025, **460**, 115486.
17 S. R. El-ezbawy and M. A. Alshaikh, *Phosphorus, Sulfur Silicon Relat. Elem.*, 1990, **48**, 111–116.
18 L. Yurttaş, B. K. Çavuşoğlu and Z. Cantürk, *Synth. Commun.*, 2020, **50**, 3072–3079.
19 E. dos, A. dos Santos, E. Hamel, R. Bai, J. C. Burnett, C. S. S. Tozatti, D. Bogo, R. T. Perdomo, A. M. M. Antunes, M. M. Marques, M. de, F. C. Matos and D. P. de Lima, *Bioorg. Med. Chem. Lett.*, 2013, **23**, 4669–4673.

20 C. D. Prasad, S. J. Balkrishna, A. Kumar, B. S. Bhakuni, K. Shrimali, S. Biswas and S. Kumar, *J. Org. Chem.*, 2013, **78**, 1434–1443.
21 W.-Y. Zhou, M. Chen, P.-Z. Zhang, A.-Q. Jia and Q.-F. Zhang, *J. Chem. Crystallogr.*, 2021, **51**, 301–310.
22 H. Konishi, Y. Aoki, M. Yamaguchi and K. Manabe, *ACS Catal.*, 2024, **14**, 15348–15355.
23 M. A. Fernández-Rodríguez, Q. Shen and J. F. Hartwig, *J. Am. Chem. Soc.*, 2006, **128**, 2180–2181.
24 A. Tangerman and E. G. Winkel, *Phosphorus, Sulfur Silicon Relat. Elem.*, 2013, **188**, 396–402.
25 L. A. Komarnisky, R. J. Christopherson and T. K. Basu, *Nutrition*, 2003, **19**, 54–61.
26 L. A. Komarnisky and T. K. Basu, in *Reviews in Food and Nutrition Toxicity*, ed. V. R. Preedy and R. R. Watson, CRC Press, 2005, vol. 4.
27 M. B. Gawande, P. S. Branco and R. S. Varma, *Chem. Soc. Rev.*, 2013, **42**, 3371.
28 R. B. N. Baig and R. S. Varma, *Chem. Commun.*, 2013, **49**, 752–770.
29 A. R. Sardarian, M. Zangiabadi and I. D. Inaloo, *RSC Adv.*, 2016, **6**, 92057–92064.
30 I. D. Inaloo and S. Majnooni, *Eur. J. Org. Chem.*, 2019, 6359–6368.
31 G. Xiang, L. Li, X. Jiang, L. He and L. Fan, *Anal. Lett.*, 2013, **46**, 706–716.
32 B. B. Sharafi, Z. J. Javidi and S. Adrangi, *Iran. J. Pharm. Res.*, 2018, **17**, 386–395.
33 I. Dindarloo Inaloo, S. Majnooni, H. Eslahi and M. Esmaeilpour, *Mol. Catal.*, DOI: 10.1016/j.mcat.2020.110915.
34 A. M. Abu-Dief and I. M. A. Mohamed, *Beni-Suef Univ. J. Basic Appl. Sci.*, 2015, **4**, 119–133.
35 A. T. Ali, M. A. Guda, A. I. Oraibi, I. K. Salih, A. H. Shather, A. T. Abd Ali, A. L. Azzawi and H. A. Almashhadani, *RSC Adv.*, 2023, **13**, 22538–22548.
36 C. Sambiagio, S. P. Marsden, A. J. Blacker and P. C. McGowan, *Chem. Soc. Rev.*, 2014, **43**, 3525–3550.
37 V. Ruta, G. Di Liberto, F. Moriggi, Y. P. Ivanov, G. Divitini, G. Bussetti, V. Barbera, M. A. Bajada, M. Galimberti, G. Pacchioni and G. Vilé, *ChemSusChem*, DOI: 10.1002/cssc.202301529.
38 S.-Q. Yu, N. Liu, M.-G. Liu and L. Wang, *J. Chem. Res.*, 2021, **45**, 237–241.
39 X. Xu, W. Wang, L. Lu, J. Zhang and J. Luo, *Catal. Lett.*, 2022, **152**, 3031–3045.
40 I. E. Chicea D. C. M. Cretu.
41 W. Stöber, A. Fink and E. Bohn, *J. Colloid Interface Sci.*, 1968, **26**, 62–69.
42 D. Elhamifar, P. Mofatehnia and M. Faal, *J. Colloid Interface Sci.*, 2017, **504**, 268–275.
43 Y. Ye, Z. Liu, W. Liu, D. Zhang, H. Zhao, L. Wang and X. Li, *Chem. Eng. J.*, 2018, **348**, 940–951.
44 Y. Ye, H. Zhao, C. Wang, D. Zhang, H. Chen and W. Liu, *Appl. Surf. Sci.*, 2018, **457**, 752–763.
45 Z. Liu, D. Yuan and Y. Su, *Catal. Lett.*, 2023, **153**, 698–712.
46 G. H. Du, Z. L. Liu, X. Xia, Q. Chu and S. M. Zhang, *J. Sol-Gel Sci. Technol.*, 2006, **39**, 285–291.
47 N. U. Ain, Z. U. Rehman, U. Nayab, J. A. Nasir and A. Aamir, *RSC Adv.*, 2020, **10**, 27377–27386.
48 S. A. H. Ichie, *Nanomater. Chem.*, 2023, **1**, 32–45.
49 Z. Shirvandi and A. Rostami, *Appl. Organomet. Chem.*, DOI: 10.1002/aoc.7321.
50 A. Ghorbani-Choghamarani, Z. Moradi and G. Azadi, *J. Sulfur Chem.*, 2018, **39**, 237–251.
51 H. Jin, P. Liu, Q. Teng, Y. Wang, Q. Meng and C. Qian, *Int. J. Mol. Sci.*, 2022, **23**, 15360.